PIER C

NGD Bandpass Type Characterization of Circular Curved Coupled-Line

Xirui Wang[1], Fayu Wan[1, *], Vladimir Mordachev[2], Eugene Sinkevich[2],
Samuel Ngoho[3], Nour M. Murad[4], and Blaise Ravelo[1]

[1]*Nanjing University of Information Science & Technology (NUIST), Nanjing 210044, Jiangsu, China*
[2]*R&D Laboratory of EMC, BSUIR, Minsk, Belarus*
[3]*Association Française de Science des Systèmes (AFSCET), Paris, France*
[4]*Piment Laboratory, Network and Telecom Department, IUT, Univ. La Réunion, Saint-Pierre, France*

ABSTRACT: The present study examines the negative group delay (NGD) behavior of a circular curved (CC) coupled-line (CL) microstrip circuit with a bandpass (BP) characteristic. The novel CC CL-based circuit is derived from the curved li-topology which demonstrates BP-NGD functionality. The basic theoretical approach enabling the BP-NGD analysis is introduced. The BP-NGD function main properties related to NGD center frequency, NGD value, and NGD bandwidth are defined. Despite the progressive NGD research work, it was wondered how the RF printed circuit board trace geometrical parameters such as curvature radius and angle change the microwave communication parameters. To verify the BP-NGD concept feasibility, different microstrip prototypes are designed, simulated, fabricated, and tested as the proof of concept (POC). Thus, a developed empirical study of CC microstrip structures corroborating well-correlated simulations and experimental results is examined. Moreover, deep sensitivity analyses for geometrical design parameters were performed using commercial tool full-wave simulations. The obtained results provide insights into the effects of CC-structure inter-space and curvature angles on the inherent BP-NGD parameters. The proposed NGD circuit is potentially useful in the future in RF and microwave engineering for signal delay correction. Additionally, it helps in understanding the characteristics of microstrip PCB traces that are important for optimizing signal integrity (SI), power integrity (PI), and electromagnetic compatibility (EMC).

1. INTRODUCTION

The contemporary challenge in the present era lies in the design and fabrication of advanced electronic printed circuit boards (PCBs), which have become increasingly arduous due to the escalation of integration density [1, 2]. To meet the requirement of high integration density, the PCB design complexity is constantly increasing. Behind the outstanding technological progress, undesired crosstalk is generated in PCB electrical interconnects [3–5]. Hence, apart from the design approach, additional investigation is essential in the domains of signal integrity (SI), power integrity (PI), and electromagnetic compatibility (EMC) [6–8]. Against the SI, PI, and EMC issues, PCB simulation tools based on 2-D or 3-D electromagnetic (EM) computation were developed [9, 10]. Different families of numerical computation methods were considered to develop relevant computer-aided design (CAD) solvers for the PCB interconnect effect prediction [11]. Commercial simulation tools for PCB analyses have been developed thanks to extensive CAD exploration [12–14]. However, most of these 2-D/3-D computational solvers of the available commercial tools [12–14] do not enable us to understand the electrical and EM phenomena behind the SI, PI, and EMC issues due to the PCB interconnect complexity. In addition to the design complexity, the interconnect PCB simulations are mostly excessively time-consuming. Only with the 2-D/3-D EM computations, the full wave mesh-

ing does not enable us to analytically highlight the main causes of interconnect propagation delays. To overcome the limitation on the electrical effect understanding, we can proceed with the PCB interconnect analyses based on the transmission line (TL) theory [15–18]. Further PCB interconnect modeling research must be performed to develop relevant methods for estimating EM coupling, attenuation, and delays or to treat the previously discussed SI and EMC issues [3–8]. For fast estimation of the interconnect delay, various lumped element-based circuit models were introduced [19–23]. To take into account the inductive effects, a more precise TL lumped RLC-model was suggested for the analysis of PCB SI [19 20]. The model of PCB interconnect time delay was unified through the exploitation of the RLC-approach [20–22]. A more precise algebraic equation was established for the calculation of interconnect delay [21]. Additionally, the buffered interconnect trees were optimized using this approach [22]. Further investigations are imperative to gain deeper insights into PCB interconnect at higher frequencies, despite the existence of lumped RC- and RLC-model developments. More advanced interconnect models based on the distributed TL were introduced [18, 23, 24]. Analytical expressions of the suitable transfer function [23] and S-parameters [24] for microstrip PCB interconnect were established by taking into account the characteristic impedance and propagation constants. In addition to the signal distribution properly through the isolated interconnects, the EMC researchers may encounter some novel and unfamiliar phenom-

ena related to the group delay, which could pose unresolved questions. Although there has been some progress on the interconnect analytical modeling, further studies must be performed for deeper understanding regarding the effect of PCB interconnect crosstalk [3–8, 25].

Several singular physical effects due to the PCB interconnect crosstalk still need to be highlighted. For example, most EMC PCB design engineers have limited understanding of the negative group delay (NGD) phenomenon, which is often observed in PCB microstrip interconnects. Further research work is needed for the physical interpretation of NGD effect. Doing this, bandpass (BP) NGD circuits (NGDCs) were proposed by exploiting some structures of interconnect PCBs [26–29]. The BP-NGD effect was investigated with distributed transmission line (TL) [26], radial stub ended CL [27], lumped circuits [28], and lossy coupling [29]. It is found that for the coupler-based NGD topology, when the resonator is close to the microstrip transmission line, the NGD phenomenon can be observed due to the positive and negative interference between the direct and coupled signals from input to output ports. More recently, the NGD generator was integrated into the PCB interconnects using signal interference methods [30]. Additionally, recent research indicates that the BP-NGD functions have the potential to enhance RF and microwave operations [31–33]. A novel approach, based on the BP-NGD equalization technique, is introduced in [34–36] to mitigate the adverse effects of EM interference resonance. Moreover, it is crucial to conduct further analytical inquiries in order to attain a comprehensive understanding of the BP-NGD effect arising from interconnects coupling. Consequently, the present investigation aims to explore the impact of BP-NGD on crosstalk coupling in PCB trace structures, specifically focusing on typical circular curved (CC) shaped microstrip traces [37]. The proof of concept (POC) circuit consists of a victim folded two-port TL, and another coupled TL is placed in its proximity. The paper consists of four main sections as follows:

- Section 2 mainly emphasizes theoretical analysis. The basic definition of BP-NGD function is introduced. Then, the essential equations about the parameters of the li-topology as a BP-NGD function are recalled.

- In Section 3, the design and prototyping of the BP-NGD CC-circuits as proof of concept (POC) are described.

- Section 4 presents different outcomes from experimental analysis conducted on microstrip circuits based on CC CL. The results of calculation, simulation, and test are compared and discussed.

- Then, Section 5 is the final conclusion.

2. BP-NGD THEORETICAL APPROACH OF LI-TOPOLOGY

After the analytical description of the S-matrix investigation concerning li-topology [38], this section presents the BP-NGD effect specifications.

2.1. *S*-Parameter Description

The analytical description of the considered BP-NGD circuit is elaborated according to the microwave theory. Like the classical circuits, the S-parameter analysis is the fundamental approach for the BP-NGD microstrip structures [26, 27]. Fig. 1 illustrates the studied passive li-topology as a two-port circuit [38].
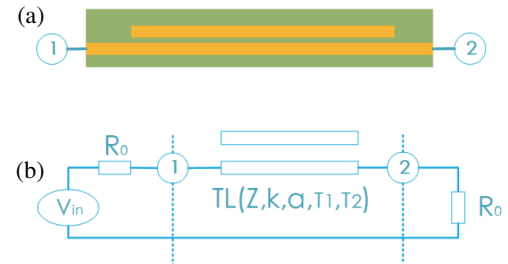
FIGURE 1. (a) 2-D microstrip design and (b) equivalent circuit of li-topology [38].

In this diagram, $R_0 = 50\,\Omega$ denotes the reference impedance. The characteristic impedance (Z), attenuation loss (a), and propagation delays (τ_1 and τ_2) describe the CL. The coupling coefficient (k), with a value between 0 and 1, and the delay of the signal propagating through the CL (τ_1 and τ_2) define the equivalent CL model. In terms of S-parameters, the associated model can be expressed as:

$$[S_{NGD}(j\omega)] = \begin{bmatrix} S_{11}(j\omega) & S_{12}(j\omega) \\ S_{21}(j\omega) & S_{22}(j\omega) \end{bmatrix} \quad (1)$$

For the case of the symmetric passive circuit, the input and output reflection coefficients $S_{11} = S_{22}$, and the forward and backward transmission coefficients $S_{12} = S_{21}$ are identical:

$$S_{mn}(j\omega) = S_{nm}(j\omega) = [rN_{mn}(\omega) + j \cdot iN_{mn}(\omega)]/ \\ [rD_{mn}(\omega) + j \cdot iD_{mn}(\omega)] \quad (2)$$

where Z-real part $real(Z) = rX$, Z-imaginary part $imag(Z) = iX$, $numerator(S_{mn}) = N_{mn}$ and $denominator(S_{mn}) = D_{mn}$ with $j^2 = -1$ and $m, n = \{1, 2\}$. The S-parameter magnitudes defined by $S_{mn}(\omega) = |S_{mn}(j\omega)|$ can be expressed as:

$$S_{mn}(\omega) = \sqrt{[rN_{mn}^2(\omega) + iN_{mn}^2(\omega)]/[rD_{mn}^2(\omega) + iD_{mn}^2(\omega)]} \quad (3)$$

2.2. BP-NGD Fundamental Specifications

By taking the transmission phase $\varphi(\omega) = \arg[S_{21}(j\omega)]$, the GD analysis is based on the relation:

$$GD(\omega) = -\partial\varphi(\omega)/\partial\omega \quad (4)$$

The BP-NGD function behavior is introduced by Fig. 2(a). $\omega_n = 2\pi f_n$ is the NGD center frequency. The lower (f_1) and upper (f_2) NGD cut-off frequencies ($\omega_{1,2} = 2\pi f_{1,2}$) are defined by:

$$GD(\omega_1) = GD(\omega_2) = 0 \quad (5)$$
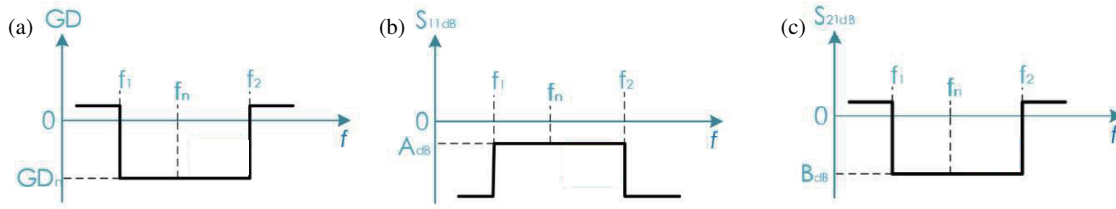
FIGURE 2. BP-NGD effect (a) GD, (b) S_{11}, and (c) S_{21} typical responses.

TABLE 1. CC-circuit employed substrate parameters.

Designation	Name	Value
Thickness	h	1.6 mm
Relative permittivity	ε_r	4.2
Metallization thickness	t	35 μm
Loss tangent	$\tan(\delta)$	0.02
Metallization conductivity	σ	58 MS/m

The NGD bandwidth indicated by Fig. 2 is equal to:

$$BW = f_2 - f_1 = (\omega_2 - \omega_1)/(2\pi) \qquad (6)$$

The NGD value by negative real parameter is analytically defined by:

$$GD(\omega_n) = GD_n < 0 \qquad (7)$$

It is very important to keep in mind that the ideal response expected to BP-NGD function illustrated in Fig. 2(a) is defined by the following ideal condition with the NGD frequency band:

$$GD(\omega) \approx GD_n \qquad (8)$$

It means that outside the NGD the frequency band, the GD must be positive under condition $GD(\omega) > 0$. Knowing the GD specifications and NGD frequency band, the insertion and reflection loss specifications also need to be recalled. As shown in Fig. 2(b) and Fig. 2(c), the main S-parameters to be considered for the li-topology NGD analysis are reflection and transmission coefficients similar to the classical millimeter wave circuit constraints. As seen in Fig. 2(b), within the NGD frequency band, the li-topology access matching must respect constraints quantified by the real positive value $S_{11}(\omega) \leq S_{11_{\max}} = A = 10^{A\,\mathrm{dB}/20}$. Fig. 2(c) represents the constraint of li-topology insertion loss $S_{21}(\omega) \geq S_{21_{\min}} = B = 10^{B\,\mathrm{dB}/20}$.

2.3. li-Topology BP-NGD Specification

The li-topology BP-NGD specifications were recently investigated [38]. The NGD center frequency is:

$$\omega_n = 1/(2\tau_1) \qquad (9)$$

By taking positive real $k_0 = \sqrt{1 - k^2}$, the NGD value $GD_n = GD(\omega_n)$ at the center frequency can be expressed by:

$$GD_n = \tau_2 \left[\left(1 + a^2 k_0^2\right)^2 - 2k^2 \right] / \left[k_0^2 \left(1 + a^2\right) \left(1 + a^2 k_0^2\right) \right] \qquad (10)$$

This NGD value is negative when:

$$k \geq k_{\min} = \sqrt{1 + \frac{1 + a^2 - \sqrt{1 + 2a^2 + 2a^4}}{a^4}} \qquad (11)$$

The S_{11} and S_{21} of the li-topology at the NGD center-frequency are respectively:

$$S_{11}(\omega_n) = k^2/[1 - a^2(1 - k^2)] \qquad (12)$$

$$S_{21}(\omega_n) = \frac{k_0^2 a \sqrt{k^2(1+a^4)(1+k^4) + 2k^2 a^2 + 2a^2(k^4 - 1) + k_0^2 \cos(\pi\tau_1/\tau_2)}}{1 - a^2 k_0^2} \qquad (13)$$

As POC of BP-NGD implemented in CC microstrip planar technology, the description of the design and prototyping approaches are presented in the next section.

3. DESCRIPTION OF CC-MICROSTRIP CIRCUIT DESIGNING AND PROTOTYPING

The present section addresses the designed and prototyped POC CC-circuit representing the curved CL of li-topology as a BP-NGD function.

3.1. Description of CC-Circuit POCs

The CC-circuit POCs are designed as 2-D structures in the environment of the commercial tool HFSS® from Ansys® and implemented in microstrip technology. Fig. 3(a) and Fig. 3(b) illustrate the 2-D geometrical design of the CC-circuits with intercept curvature angle deg $= 180°$ and deg $= 90°$, respectively. The different cases of CC-circuit HFSS® design are viewed in Figs. 3(c), 3(d), and 3(e). Table 1 illustrates the characteristics of the Cu-metallized FR4 epoxy dielectric substrate that is used for the printed POCs.

The disparities between the GD and S-parameter responses predominantly stem from the bending characteristics of the CC-structure.

The CC-microstrip circuit prototypes were fabricated to verify the BP-NGD response behaviors as described in the next paragraph.
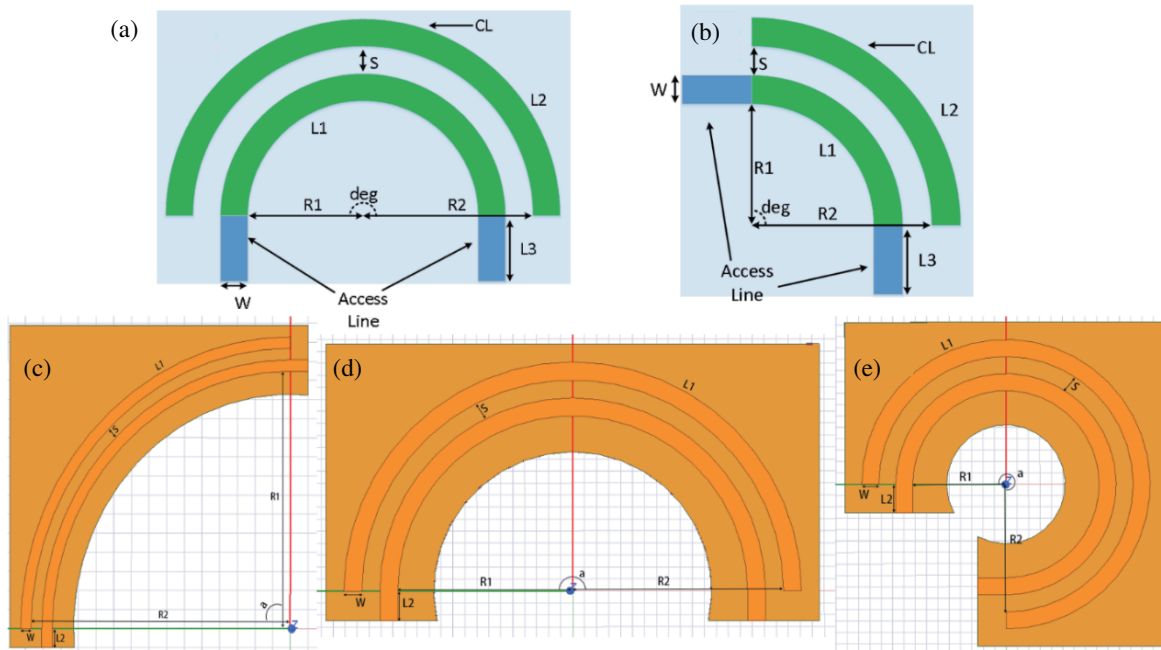
FIGURE 3. CC-structure geometrical design: (a) deg $= 180°$ and (b) deg $= 90°$. HFSS® planar design with (c) deg $= 90°$, (d) deg $= 180°$ and (e) deg $= 270°$.
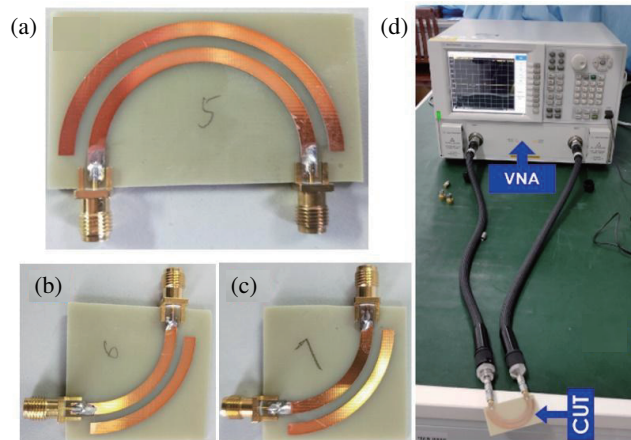
FIGURE 4. Fabricated CC-microstrip circuit prototypes: (a) (deg $= 180°$, $s = 2.5$ mm), (b) (deg $= 90°$, $s = 2.5$ mm) and (c) (deg $= 90°$, $s = 2.2$ mm). (d) CC-microstrip circuit experimental setup.

TABLE 2. Geometrical parameters of CC-circuit prototypes shown in Fig. 4.

Designation	Parameters	Fig. 4(a)	Fig. 4(b)	Fig. 4(c)
Size	Width×Length	35 mm×60 mm	35 mm×35 mm	35 mm×35 mm
Access line	w		3 mm	
	L_3		5 mm	
CL	R_1		20 mm	
	R_2	25.5 mm	25.5 mm	25.2 mm
	s	2.5 mm	2.5 mm	2.2 mm
	L_1	67.54 mm	33.78 mm	33.78 mm
	L_2	84.82 mm	42.41 mm	41.94 mm
	deg	180°	90°	90°
	Z_1		50 Ω	
	k	-21.52 dB	-21.52 dB	-20.36 dB
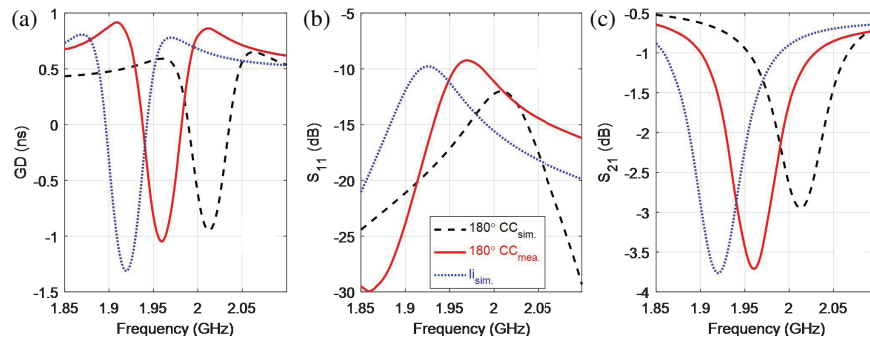
FIGURE 5. Comparison of li- and CC-structure simulations and measurements: (a) GD, (b) S_{11} and (c) S_{21} of the 180°-CC prototype shown in Fig. 4(a).

TABLE 3. BP-NGD parameters from li- and CC-structure simulations and measurements.

Approach	f_n (GHz)	GD_n (ns)	$S_{21}(f_n)$ (dB)	$S_{11}(f_n)$ (dB)
li-circuit simulation	1.926	-1.36	-3.68	-9.98
CC-circuit simulation	2.120	-0.98	-2.96	-12.10
CC-circuit measurement	1.961	-1.05	-3.71	-9.52

3.2. Description of Fabricated CC-Circuit Prototypes

Figures 4(a), 4(b), and 4(c) display the fabricated circuit prototypes. The constituting geometrical element specifications of each prototype are given in Table 2. Fig. 4(d) presents the experimental setup of the CC-NGD circuit, using a two-port Vector Network Analyzer (VNA).

During the experimental test, the VNA test equipment provided by Rohde&Schwarz®referenced ZNB 20, which operates in the frequency range of 100 kHz to 20 GHz, was utilized. The S-parameter investigation was performed in the frequency band defined from 1.8 GHz to 2.1 GHz. The obtained BP-NGD results of the CC-circuits are examined in the next section.

4. VALIDATION RESULTS FROM CC-CIRCUIT EXPERIMENTAL INVESTIGATION

To illustrate more quantitatively the BP-NGD effect related to the CC-circuit representing the curved li-topology, experimentations were performed. The results from the experimentation and S-parameter simulations were parallelly generated from HFSS® 3-D EM simulator software. The following subsections interpret the obtained empirical results with a comparison of simulated ones.

4.1. Validation Results of 180°-CC Circuit

In this paragraph, we examine the comparisons of results from HFSS®simulation ("CC-Simu." plotted in black dashed lines and "li-Simu." plotted in blue dotted lines) and measurement ("Meas." plotted in red solid lines) results, which are derived from the 180°-CC circuit shown in Fig. 4(a). In addition, the equivalent li-circuit considered in this study is shown in Fig. 1(a). Fig. 5 displays the acquired findings. Within the 180°-CC circuit, the dimensions of length $L2$ and interspace match the length and spacing of the li-circuit. It can be seen

that the simulation and measurement results are in good agreement. As expected, according to the GD plot seen in Fig. 5(a), it is noteworthy that the properties of the tested 180°-CC circuit accord with the characteristics of BP-NGD. Fig. 5(b) and Fig. 5(c) denote the comparisons of the reflection coefficients ($S_{11\,\mathrm{dB}}$) and the transmission coefficients ($S_{21\,\mathrm{dB}}$), respectively. As depicted in Fig. 5(a), a slight disparity can be observed in the simulated GD responses between the 180°-CC circuit and li-circuit. The analysis of Table 3 reveals that the NGD center frequency simulation result of the 180°-CC circuit is about 2.12 GHz, whereas the li-circuit is about 1.926 GHz. A disparity of roughly 194 MHz can be discerned between the two NGD central frequencies.

4.2. Simulated and Experimental Results of 90°-CC Circuits

The BP-NGD validation results of 90°CC-prototypes designed with two different values of spaces $s = 2.5\,\mathrm{mm}$ and $s = 2.2\,\mathrm{mm}$ highlighted by Fig. 6 and Fig. 7, respectively, are explored in the present paragraphs. We examine the comparisons of results from HFSS© simulation ("CC-Simu." plotted in black dashed lines and "li-Simu." plotted in blue dotted lines) and measurement ("Meas." plotted in red solid lines) results, which are derived from the 90°-CC circuit shown in Fig. 4(b) and Fig. 4(c). Slight differences between the BP-NGD characteristics are observed. Therefore, we can develop much more in detail, for example, the comments on the GD and S-parameter responses of Fig. 6 to interpret the obtained 90°CC-circuit results. Fig. 6 depicts the case of study concerning the prototype of the 90°-CC circuit introduced by the design of Fig. 4(c). We can emphasize once again, from the results plotted in Fig. 6, that simulations and measurements are in good agreement.

The GD response displayed in Fig. 6(a) highlights the confirmation of the BP-NGD behavior under study. Fig. 6(b) and Fig. 6(c) represent the measured and simulated $S_{11\,\mathrm{dB}}$ and
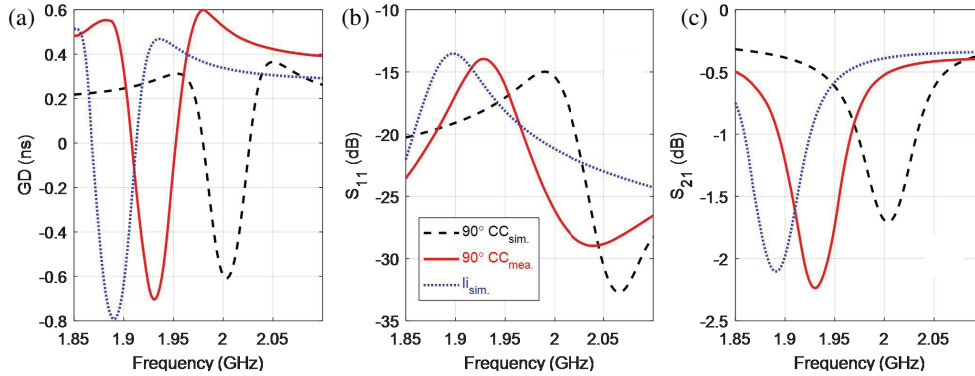
FIGURE 6. Comparison of li- and $90°$-CC-structure simulations and measurements with $s = 2.5$ mm: (a) GD, (b) S_{11}, and (c) S_{21} of the $90°$-CC prototype shown in Fig. 4(c).
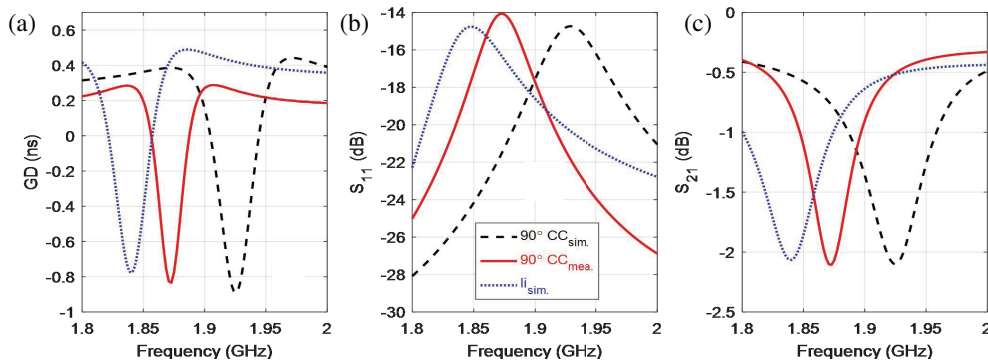
FIGURE 7. Comparison of li- and $90°$CC-structure simulations and measurements with $s = 2.2$ mm: (a) GD, (b) S_{11} and (c) S_{21} of the $90°$CC prototype shown in Fig. 4(b).

TABLE 4. li- and $90°$CC-structure simulated and measured results.

Approach	s (mm)	f_n (GHz)	GD_n (ns)	$S_{21}(f_n)$ (dB)	$S_{11}(f_n)$ (dB)
li-circuit simulation		1.888	-0.78	-2.10	-13.54
CC-circuit simulation	2.5	2.000	-0.61	-1.70	-15.00
CC-circuit measurement		1.930	-0.70	-2.23	-13.90
li-circuit simulation		1.847	-0.75	-2.06	-15.20
CC-circuit simulation	2.2	1.926	-0.89	-2.10	-14.80
CC-circuit measurement		1.870	-0.82	-2.10	-14.70

$S_{21\,\text{dB}}$, from the $90°$-CC circuit prototype, respectively. Table 4 summarizes the comparison of the corresponding BP-NGD characteristics. For the considered $90°$CC-circuit, the NGD level is about -0.608 ns around the center frequency 2 GHz.

Compared to the previous case of $180°$CC-circuit, in this case, the NGD absolute value is significantly reduced. Moreover, we can also find a significant NGD central frequency shift about 70 MHz between the simulation model and measured results.

The BP-NGD responses for the case of $90°$CC-circuit designed with interspace $s = 2.2$ mm are given in Fig. 7, and the associated characteristics are summarized in Table 4. We can underline that the NGD absolute value is slightly increasing

and the reflection coefficient slightly worse than for the case of $s = 2.5$ mm. For a better understanding of the curvature effect on the li-topology, a sensitivity study in the function of space and intercept angle was performed. The following subsection explores the innovative results.

4.3. Full-Wave Simulation Based-Sensitivity Analyses of the CC-Structures

To analyze the influence of s and deg on the microwave response of the CC-structure, we conducted parametric analyses. The simulation results used for the analysis were simulated using HFSS® with a frequency variation range of 1.8–2.3 GHz.
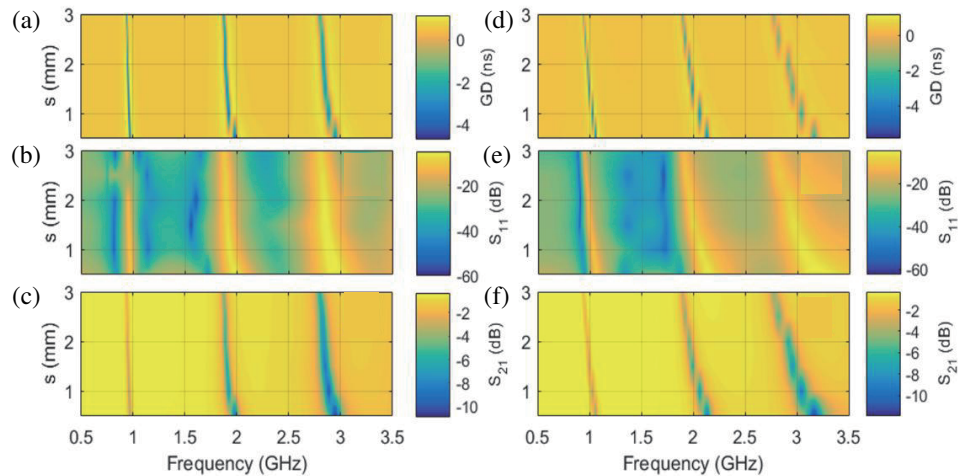
FIGURE 8. Mappings of: $180°$CC-structure: (a) GD, (b) S_{11} and (c) S_{21} versus (f, s), and li-structure (d) GD, (e) S_{11} and (f) S_{21} versus (f, s).

TABLE 5. BP-NGD characteristics versus s.

Structure	s (mm)	f_n (GHz)	GD_n (ns)	$S_{21}(f_n)$ (dB)	$S_{11}(f_n)$ (dB)
CC	0.5	2.173	-4.04	-9.04	-4.62
li	0.5	2.153	-3.56	-7.50	-5.72
CC	1	2.104	-3.52	-7.17	-6.02
li	1	2.074	-3.36	-6.64	-6.42
CC	1.5	2.030	-3.21	-6.06	-7.17
li	1.5	2.007	-3.30	-6.26	-6.80
CC	2	2.001	-2.74	-5.04	-8.41
li	2	1.969	-1.88	-5.40	-7.94
CC	2.5	1.960	-2.27	-4.13	-9.96
li	2.5	1.926	-2.55	-4.68	-8.87
CC	3	1.935	-1.86	-3.42	-11.52
li	3	1.886	-2.30	-4.21	-9.67

4.3.1. Sensitivity Analysis Versus s

In the process of conducting HFSS® parametric simulation, the range of linear variation for the s of the $180°$CC-circuit spanned from 0.5 mm to 3 mm. Fig. 8 represents the mappings of CC- and li-circuit GD response and corresponding S_{11} and S_{21} versus s, respectively. According to Figs. 8(a) and 8(d), we can ascertain the impact of the CL physical interspace on the BP-NGD function: (i) as the space increases, the NGD center frequency decreases; (ii) the absolute value of the NGD also decreases; and (iii) the NGD bandwidth decreases as well. As shown in Table 5, f_n of the $180°$CC-circuit decreases from 2.173 GHz to 1.935 GHz when increasing s from 0.5 mm to 3 mm which is compared to li-results shown in Figs. 8(d), 8(e), and 8(f). At the same time, the NGD value varies between -1.86 ns and -4.04 ns. As addressed by Table 5, the attenuation loss is kept between 3.42 dB and 9.04 dB. Hence, within the range of CL interspace variation, the reflection coefficient is kept between -4.62 dB and -11.52 dB.

4.3.2. Sensitivity Analysis Versus Curvature Angle

The present sensitivity analysis is based on arbitrary intercept angle CC-structure. In this case of study, we conducted parametric simulations using the identical frequency range as discussed in the preceding paragraph, but this time focusing on the variation of angle *deg*. The simulations were performed using HFSS® CC-circuit design, as displayed in Fig. 9. To conduct a sensitivity analysis, we linearly modified the angle *deg* of the CC-circuit from $90°$ to $180°$. Fig. 9(a) shows the change in GD response when the physical angle changes. Additionally, Fig. 10(a) shows the GD mapping from the li-structure versus length L.

Based on the findings illustrated in Fig. 9(a), it is evident that (i) as the *deg* increases, the absolute value of NGD also increases, (ii) but the center frequency of NGD decreases, and (iii) the NGD bandwidth decreased with the angle. As shown in Table 6, the NGD center frequency, f_n, of the CC-circuit varies from 3.802 GHz to 1.96 GHz when *deg* increases from $90°$ to
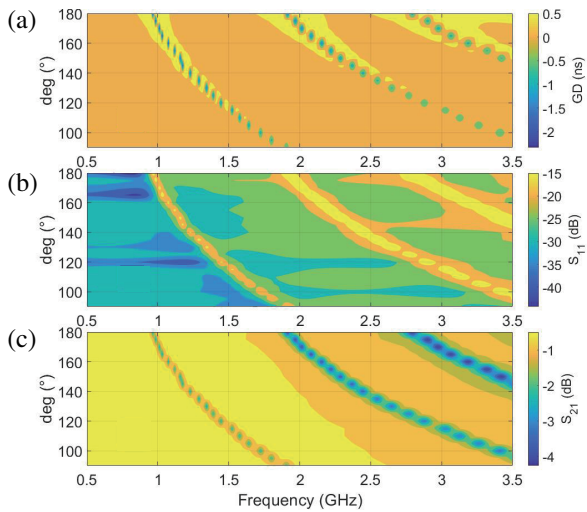
FIGURE 9. 180°CC-structure (a) GD, (b) S_{11}, and (c) S_{21} versus (f, deg).
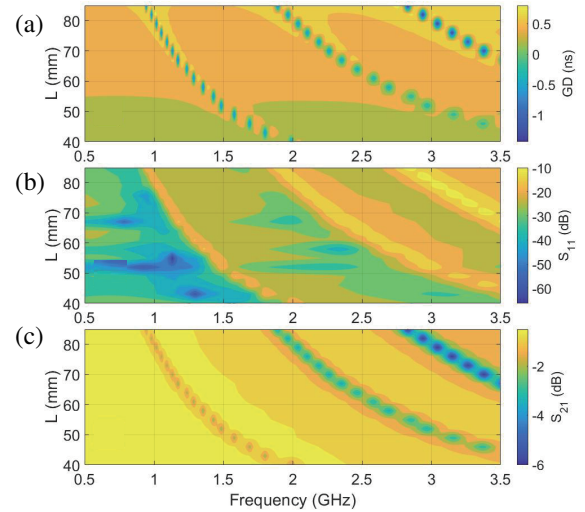
FIGURE 10. li-structure (a) GD, (b) S_{11} and (c) S_{21} versus (f, L).
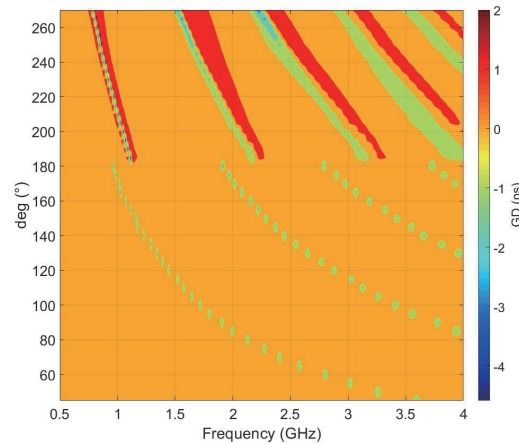
FIGURE 11. CC-structure simulation results of GD versus (f, deg).

TABLE 6. BP-NGD characteristics versus angle.

Structure	Varied parameter	f_n (GHz)	GD_n (ns)	$S_{21}(f_n)$ (dB)	$S_{11}(f_n)$ (dB)
CC	deg= 90°	3.802	−0.68	−3.79	−10.67
li	$L = 42.41$ mm	3.750	−0.99	−4.35	−9.59
CC	deg= 105°	3.351	-0.96	-3.78	-10.45
li	$L =49.48$ mm	3.250	−1.30	−4.61	−8.90
CC	deg= 120°	2.923	−1.20	−3.81	−10.67
li	$L = 56.55$ mm	2.860	−1.59	−4.64	−8.98
CC	deg= 135°	2.631	−1.43	−3.89	−10.37
li	$L = 63.62$	2.541	−1.87	−4.68	−8.95
CC	deg= 150°	2.371	−1.69	−3.87	−10.39
li	$L = 70.69$ mm	2.298	−2.10	−4.67	−8.90
CC	deg= 165°	2.167	−2.00	−3.93	−10.28
li	$L = 77.96$ mm	2.095	−2.31	−4.65	−9.02
CC	deg= 180°	1.960	−2.27	−4.13	−9.96
li	$L = 84.82$ mm	1.926	−2.55	−4.68	−8.87

180°. Then, the NGD value of the curved CC-circuit varies between -0.68 ns to -2.27 ns.

The reflection and transmission coefficients are mapped in Fig. 9(b) and in Fig. 9(c) for CC-circuit and Fig. 10(b) and in Fig. 10(c) for li-circuit, respectively. We can point out that the CC-circuit attenuation loss is kept between 3.79 dB and 4.13 dB with the reflection coefficient still lower than -9.9 dB.

Furthermore, through additional full-wave simulations of the CC-circuit, we were able to expand the range of intercept angles (from $deg_{min} = 45°$ to $deg_{max} = 270°$ with a step of $deg_{step} = 5°$ which facilitated the refinement of the BP-NGD parameter f_n and GD_n. The results of the parameter sweep are shown in Fig. 11. The parametric simulation results indicate that the NGD center frequency decreases as the angle increases. However, the NGD absolute value increases as the angle increases.

5. CONCLUSION

There is currently a scarcity of scientific research on the impacts of PCB trace curvature on CL crosstalk within the field of EMC studies. The present study aims to elucidate the influence of geometrical parameters, such as the angle and interspace of CL, on the unfamiliar BP-NGD responses. In the initial step, the fundamental attributes of the unfamiliar BP-NGD reactions are recalled. Subsequently, the electrical variables are utilized to present the BP-NGD parameters about li-topology. To demonstrate the impact of curvature, we examine the circular traces of microstrip interconnects. By conducting both numerical and experimental analyses, we investigate the novel BP-NGD of prototypes with 180° and 90° CC-circuits. The simulations were performed using a 3-D design software tool specialized in EM applications. To confirm more realistically, the influential study of the geometrical parameter effects and comparisons between simulation results and experimentations are discussed. Additionally, to enhance comprehension, sensitivity analyses were performed about the interspace and angle of the curved CL that constitutes the li-circuit. As anticipated, the variation of transmission- and reflection-coefficients, NGD frequency, NGD bandwidth, and NGD value in the CC-circuit depends greatly on the intercept angle and interspaces. In the future, the proposed research will be beneficial for electronic design engineers specializing in PCBs. It aims to forecast the behaviors of PCB traces by considering various geometrical parameters.

ACKNOWLEDGEMENT

REFERENCES

[1] Tun, L. P. and L. C. Peng, "Challenges in high density PCB with 0.40 mm pitch BGA — from design, fabrication & assembly perspective," in *2009 1st Asia Symposium on Quality Electronic Design*, 44–48, Kuala Lumpur, Malaysia, Jul. 2009.

[2] Rao, G. and N. Rao, "A web based course on designing high density interconnect PCBs for manufacturability," in *50th Electronic Components & Technology Conference — 2000 Proceedings*, 1285–1288, Las Vegas, Nv, May 2000.

[3] Frisk, L., S. Lahokallio, and J. Kiilunen, "Comparison of microvia hdi pcbs with ACF interconnections in accelerated life testing," in *2017 21st European Microelectronics and Packaging Conference (EMPC) & Exhibition*, 1–6, 2017.

[4] Sung, M., W. Ryu, H. Kim, J. Kim, and J. Kim, "An efficient crosstalk parameter extraction method for high-speed interconnection lines," *IEEE Transactions on Advanced Packaging*, Vol. 23, No. 2, 148–155, May 2000.

[5] Kim, D. and Y. Eo, "s-parameter-measurement-based time-domain signal transient and crosstalk noise characterizations of coupled transmission lines," *IEEE Transactions on Advanced Packaging*, Vol. 32, No. 1, 152–163, Feb. 2009.

[6] Fan, J., X. Ye, J. Kim, B. Archambeault, and A. Orlandi, "Signal integrity design for high-speed digital circuits: Progress and directions," *IEEE Transactions on Electromagnetic Compatibility*, Vol. 52, No. 2, 392–400, May 2010.

[7] Kim, J. and E. Li, "Special issue on PCB level signal integrity, power integrity, and EMC," *IEEE Transactions on Electromagnetic Compatibility*, Vol. 52, No. 2, 246–247, May 2010.

[8] Schuster, C. and W. Fichtner, "Parasitic modes on printed circuit boards and their effects on emc and signal integrity," *IEEE Transactions on Electromagnetic Compatibility*, Vol. 43, No. 4, 416–425, 2001.

[9] Archambeault, B., C. Brench, and S. Connor, "Review of printed-circuit-board level EMI/EMC issues and tools," *IEEE Transactions on Electromagnetic Compatibility*, Vol. 52, No. 2, 455–461, May 2010.

[10] Swirbel, T., A. Naujoks, and M. Watkins, "Electrical design and simulation of high density printed circuit boards," *IEEE Transactions on Advanced Packaging*, Vol. 22, No. 3, 416–423, Aug. 1999.

[11] Buckwalter, J. F., "Predicting microwave digital signal integrity," *IEEE Transactions on Advanced Packaging*, Vol. 32, No. 2, 280–289, May 2009.

[12] Wan, F., T. Gu, S. Lallechere, J. Nebhen, and B. Ravelo, "NGD investigation on medusa-shape interconnect structure," *International Journal of RF and Microwave Computer-aided Engineering*, Vol. 31, No. 10, Oct. 2021.

[13] available at: https://www.ansys.com/products/electronics/option-ansys-si.

[14] available at: https://www.3ds.com/productsservices/simulia/training/course-descriptions/cst-studio-suite-edasi-pi/.

[15] Ruehli, A. E. and A. C. Cangellaris, "Progress in the methodologies for the electrical modeling of interconnects and electronic packages," *Proceedings of the IEEE*, Vol. 89, No. 5, 740–771, 2001.

[16] Khan, Z. A., "A novel transmission line structure for high-speed high-density copper interconnects," *IEEE Transactions on Components Packaging and Manufacturing Technology*, Vol. 6, No. 7, 1079–1088, Jul. 2016.

[17] Branch, K. M. C., J. Morsey, A. C. Cangellaris, and A. E. Ruehli, "Physically consistent transmission line models for high-speed interconnects in lossy dielectrics," *IEEE Transactions on Advanced Packaging*, Vol. 25, No. 2, 129–135, May 2002.

[18] Ravelo, B., "Delay modeling of high-speed distributed interconnect for the signal integrity prediction," *European Physical Journal-applied Physics*, Vol. 57, No. 3, Feb. 2012.

[19] Kahng, A. B. and S. Muddu, "An analytical delay model for RLC interconnects," *IEEE Transactions on Computer-aided Design of Integrated Circuits and Systems*, Vol. 16, No. 12, 1507–1514,

1997.

[20] Venkatesan, R., J. A. Davis, and J. D. Meindl, "Compact distributed rlc interconnect models — part IV: unified models for time delay, crosstalk, and repeater insertion," *IEEE Transactions on Electron Devices*, Vol. 50, No. 4, 1094–1102, Apr. 2003.

[21] Roy, S. and A. Dounavis, "Efficient delay and crosstalk modeling of RLC interconnects using delay algebraic equations," *IEEE Transactions on Very Large Scale Integration (VLSI) Systems*, Vol. 19, No. 2, 342–346, Feb. 2011.

[22] Wang, S. L. and T. W. Chang, "Delay modeling for buffered RLY/RLC trees," in *2005 IEEE VLSI-TSA International Symposium on Vlsi Design, Automation & Test (VLSI-TSA-DAT), Proceedings of Technical Papers*, 237–240, Automation and Test, Hsinchu, Apr. 2005.

[23] Choi, M., J.-Y. Sim, H.-J. Park, and B. Kim, "An approximate closed-form transfer function model for diverse differential interconnects," *IEEE Transactions on Circuits and Systems I-regular Papers*, Vol. 62, No. 5, 1335–1344, May 2015.

[24] Eudes, T., B. Ravelo, and A. Louis, "Experimental validations of a simple pcb interconnect model for high-rate signal integrity," *IEEE Transactions on Electromagnetic Compatibility*, Vol. 54, No. 2, 397–404, Apr. 2012.

[25] Maza, M. S. and M. L. Aranda, "Analysis of clock distribution networks in the presence of crosstalk and groundbounce," in *ICECS 2001. 8th IEEE International Conference on Electronics, Circuits and Systems (CAT. No. 01ex483)*, Vol. 2, 773–776, 2001.

[26] Ngoho, S., Y. C. M. Boussougou, S. S. Yazdani, Y. Dong, N. M. Murad, and Lalléchère, "Design and modelling of ladder-shape topology generating bandpass NGD function," *IEEE Transactions on Electromagnetic Compatibility*, Vol. 62, No. 5, 1813–1821, 2020.

[27] Wan, F., L. Wu, B. Ravelo, and J. Ge, "Analysis of interconnect line coupled with a radial-stub terminated negative group delay circuit," *IEEE Transactions on Electromagnetic Compatibility*, Vol. 62, No. 5, 1813–1821, Oct. 2020.

[28] Boussougou, Y. C. M., E. J. R. Sambatra, A. Jaomiary, L. Ramifidisoa, N. M. Murad, J.-P. Kouadio, S. Ngoho, F. E. Sahoa, S. Baccar, and R. Randriatsiferana, "Bandpass-type NDG design engineering and uncertainty analysis of RLC-series resonator based passive cell," *Progress In Electromagnetics Research C*, Vol. 121, 65–82, 2022.

[29] Das, R., Q. Zhang, and H. Liu, "Lossy coupling matrix synthesis approach for the realization of negative group delay response," *IEEE Access*, Vol. 6, 1916–1926, 2018.

[30] Wang, Z., Y. Cao, T. Shao, S. Fang, and Y. Liu, "A negative group delay microwave circuit based on signal interference techniques," *IEEE Microwave and Wireless Components Letters*, Vol. 28, No. 4, 290–292, Apr. 2018.

[31] Xiao, J.-K., Q.-F. Wang, and J.-G. Ma, "Negative group delay circuits and applications: Feedforward amplifiers, phased-array antennas, constant phase shifters, non-foster elements, interconnection equalization, and power dividers," *IEEE Microwave Magazine*, Vol. 22, No. 2, 16–32, 2021.

[32] Ravelo, B., "Distributed NDG active circuit for RF-microwave communication," *AEU-international Journal of Electronics and Communications*, Vol. 68, No. 4, 282–290, 2014.

[33] Shao, T., Z. Wang, S. Fang, H. Liu, and Z. N. Chen, "A group-delay-compensation admittance inverter for full-passband self-equalization of linear-phase band-pass filter," *AEU-international Journal of Electronics and Communications*, Vol. 123, Aug. 2020.

[34] Ravelo, B., F. Wan, J. Nebhen, W. Rahajandraibe, and S. Lallechere, "Resonance effect reduction with bandpass negative group delay fully passive function," *IEEE Transactions on Circuits and Systems Ii-express Briefs*, Vol. 68, No. 7, 2364–2368, Jul. 2021.

[35] Ravelo, B., S. Lallechere, W. Rahajandraibe, and F. Wan, "Electromagnetic cavity resonance equalization with bandpass negative group delay," *IEEE Transactions on Electromagnetic Compatibility*, Vol. 63, No. 4, 1248–1257, Aug. 2021.

[36] Ravelo, B., S. Lallechere, A. Thakur, A. Saini, and P. Thakur, "Theory and circuit modeling of baseband and modulated signal delay compensations with low- and band-pass NDG effects," *AEU-international Journal of Electronics and Communications*, Vol. 70, No. 9, 1122–1127, 2016.

[37] Gu, T., X. Huang, F. Wan, B. Ravelo, and Q. Ji, "Coupled-line curvature angle effect on bandpass negative group delay characteristics," in *2022 Asia-pacific International Symposium on Electromagnetic Compatibility (APEMC)*, 458–461, 2022.

[38] Ravelo, B., L. Wu, F. Wan, W. Rahajandraibe, and N. M. Murad, "Negative group delay theory on li topology," *IEEE Access*, Vol. 8, 47 596–47 606, 2020.